Flexible Optical Tactile Sensor With CNN-Based Calibration for Robust Pressure Estimation

Ando, Kosuke

Kawaguchi, Hiroshi

Izumi, Shintaro
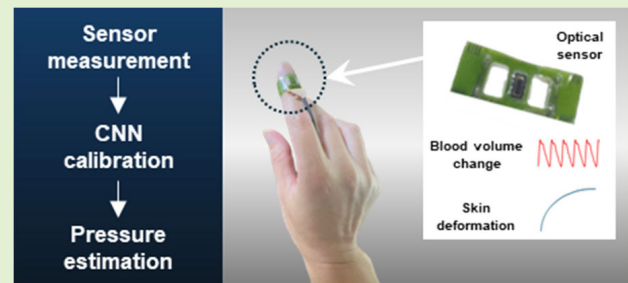
(URL)
https://hdl.handle.net/20.500.14094/0100499781

Flexible Optical Tactile Sensor With CNN-Based Calibration for Robust Pressure Estimation

Kosuke Ando⬭, Hiroshi Kawaguchi⬭, *Member, IEEE*, and Shintaro Izumi⬭, *Member, IEEE*

Abstract—**Accurately estimating pressure without interfering with natural tactile perception remains a critical challenge for wearable tactile sensors, whose outputs are often affected by attachment conditions and individual variability. Here, we present a flexible optical tactile sensor that estimates pressure from optical signals reflecting both skin deformation and hemodynamic changes. To enhance robustness and generalization across different placements and users, a convolutional neural network (CNN)-based calibration framework was developed. The sensor is less than 150 μm thick and features a perforated architecture that reduces perspiration effects while maintaining comfort and stable contact during long-term use. Experiments conducted on multiple fingers across a 0–100 kPa (0–4 N) range demonstrated stable and accurate pressure estimation, with consistent performance maintained after reattachment and across subjects. These results confirm that the CNN calibration effectively compensates for placement- and subject-dependent variability. Moreover, characteristic modulations in the optical response associated with blood-flow dynamics were observed under loading, indicating the capability to simultaneously capture mechanical and physiological information. Overall, the proposed optical tactile sensor with CNN-based calibration provides a promising platform for quantitative tactile sensing in wearable devices, human–robot interaction, and biomedical applications.**

Index Terms—**Force sensor, haptics, optical sensor, tactile.**

I. INTRODUCTION

WITH the rapid advancement of wearable devices and bioinstrumentation, there is growing interest in sensing technologies that can capture force and tactile information. In fields such as medicine, rehabilitation, sports, and robotics, noninvasive methods capable of continuously monitoring tactile cues are particularly desirable. Consequently, the human hand, rich in mechanoreceptors, has become a prominent target for tactile measurement systems [1], [2], [3]. Cutaneous mechanoreceptors distributed on and within the skin transduce physical stimuli into neural signals, forming the basis of tactile perception and enabling the discrimination of texture, temperature, and vibration [4], [5].

Conventional studies on tactile sensing have primarily focused on quantifying deformation of the finger to infer pressure and force direction. A wide variety of transduction principles have been explored, including resistive, capacitive, piezoelectric, optical, and camera-based methods [6], [7], [8], [9], [10]. Among optical approaches, several studies have estimated pressure and force direction by observing load-induced color variations in the nail bed [11], [12], [13]. However, such noninvasive techniques are typically limited to the nail or fingertip and often pose challenges in terms of wearability. In parallel, multimodal sensors that integrate tactile sensing with hand-motion tracking or pulse–wave detection modules have been developed, enabling simultaneous acquisition of mechanical and physiological signals [14], [15]. Nevertheless, these multimodal systems usually require dedicated modules for each sensing function, which increases both the device footprint and overall system complexity.

To overcome these limitations, we previously developed an optical tactile sensor with a flexible architecture that can be directly adhered to the skin and simultaneously capture skin deformation and blood-volume changes by exploiting variations in near-infrared (NIR) light scattering and absorption [16]. When mounted on the dorsum of the hand,

the sensor enables tactile-force measurement without impeding natural sensation. The device consists of an NIR light-emitting diode (LED) and a photodiode (PD) mounted on a flexible printed circuit (FPC) substrate, ensuring conformal skin contact. A portion of the emitted light is reflected at the skin surface, while the remainder penetrates into the tissue; photons that are scattered but not absorbed reemerge and are detected by the PD. External loading deforms the skin and alters both the optical path and intravascular blood volume, thereby modulating the detected optical intensity and enabling inference of applied pressure. Structurally, the device is analogous to photoplethysmography (PPG) and oxygen-saturation (SpO_2) sensors, allowing the concurrent acquisition of pulse–wave information [17], [18], [19], [20], [21]. Hence, a single noninvasive architecture can simultaneously capture mechanical and physiological signals, demonstrating both structural novelty and the potential of this approach as a foundational technology for tactile sensing.

Despite these advantages, practical implementation is still hindered by considerable variability in sensor output due to differences in placement and individual physiological factors, which complicate accurate pressure estimation. Finger size, hemodynamic state, and sensor misalignment are particularly influential; therefore, calibration is indispensable to compensate for these effects [22], [23], [24], [25].

Traditional calibration methods have relied mainly on physics-based models. While effective under controlled conditions, such approaches depend strongly on sensor geometry and material properties, and often lack generality when environmental or intersubject variations are introduced. To address this, machine-learning and deep-learning-based calibration techniques have gained attention for their ability to flexibly compensate for nonlinear and subject-dependent variability. Prior studies have applied methods such as linear regression, random forests, and support vector machines (SVMs) [26], [27]. More recently, deep learning architectures, particularly convolutional neural networks (CNNs) and recurrent neural networks (RNNs), have shown strong potential for tactile sensing applications. In particular, CNNs are well suited to scenarios involving complex physiological signals, as they efficiently extract local features from multichannel inputs and can process entire time series in parallel [28], [29], [30], [31], [32], [33].

Building on the operating principle of our flexible optical tactile sensor, this study introduces a CNN-based calibration framework that processes optical signals arising from skin deformation and hemodynamic changes to enhance the stability and accuracy of pressure estimation. By integratively analyzing deformation- and blood-flow-related signals, the CNN automatically compensates for nonlinear and subject-dependent characteristics, enabling robust and reliable pressure inference. In doing so, the proposed approach endows the optical tactile sensor with embedded calibration functionality, demonstrating its practicality as a high-precision tactile-sensing device.

Evaluations conducted across multiple fingers and subjects confirmed that the proposed sensor maintained high estimation accuracy and robustness across various loading and
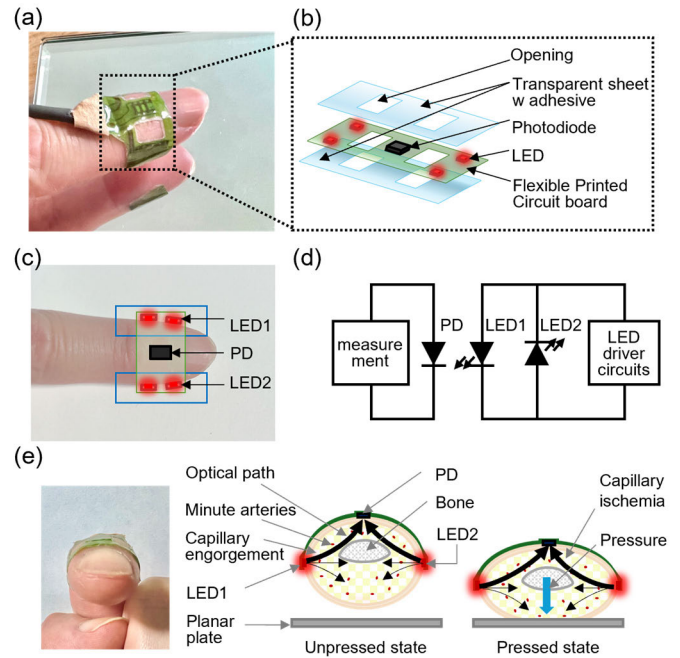

Fig. 1. Design of the flexible optical tactile force sensor. (a) Photograph showing the sensor attached to the dorsal side of the finger. (b) Layer configuration illustrating the flexible architecture of the device. (c) Arrangement of the NIR LEDs and PD used in this study. (d) Circuit configuration for LED driving and signal acquisition. (e) Schematic of the proposed sensing principle showing how applied pressure modulates optical scattering and absorption within the skin.

attachment conditions. The CNN-based calibration enabled stable pressure estimation despite differences in finger geometry, sensor placement, and individual physiology, demonstrating strong generalization and practical applicability.

By enabling simultaneous estimation of pressure and acquisition of physiological signals, the proposed approach not only improves sensing accuracy and reliability but also broadens potential applications. In clinical contexts, concurrent monitoring of contact pressure and pulse waveforms could facilitate intraoperative assessment and rehabilitation. In sports, combined analysis of grip pressure and heart rate variability may contribute to performance evaluation and fatigue detection. Looking forward, the integration of time-series analysis with multimodal learning on such multidimensional data are expected to enable deeper interpretation of human behaviors and physiological states, paving the way for an integrated tactile-sensing platform.

II. METHOD

A. Design and Implementation of the Sensor

The device developed in this study builds upon the operating principle of a flexible optical tactile sensor and integrates a calibration function to enable high-accuracy pressure estimation [Fig. 1(a)]. The sensing unit consists of a three-layer structure composed of a NIR LED and a PD mounted on a FPC substrate that conforms stably to the dorsal surface of the finger. A transparent urethane sheet is overlaid for encapsulation [Fig. 1(b)]. We employed an 860-nm LED (CSL1501RW1, Rohm Semiconductor) and a PD with a comparable peak
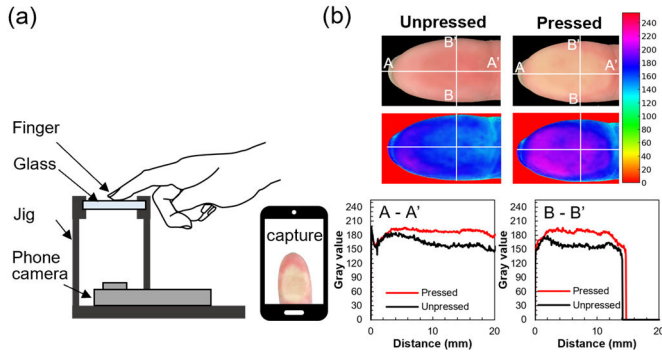
Fig. 2. Observation of optical changes under fingertip contact. (a) Experimental setup using a transparent glass plate and a fingertip contact to visualize deformation-induced optical variations. (b) Optical images and corresponding intensity profiles for unpressed and pressed states. A blurred fingerprint pattern is shown to prevent personal identification.

spectral sensitivity at 850 nm (VEMD8080CT-ND, Vishay Intertechnology). To capture the directional dependence of skin deformation, the LEDs were arranged in a circular configuration around a centrally placed PD, with a center-to-center spacing of approximately 10 mm. This geometry was optimized through prior evaluations of optical scattering characteristics in both a skin phantom and the dorsum of the hand, as described in [16].

Multiple LEDs were driven in a time-division manner to acquire direction-resolved optical signals corresponding to pressure-induced skin-tissue deformation and blood-volume changes [Fig. 1(c)]. By rapidly switching among three states, namely left-side LED on, right-side LED on, and all LEDs off, we could demultiplex the contribution of each LED while suppressing ambient-light interference through LED-on/LED-off differencing [Fig. 1(d)]. The LED and PD exhibit response times shorter than 10 μs, allowing sensor operation at a sampling rate of approximately 10 kHz. The optical path and detection conditions differ between unloaded and loaded states [Fig. 1(e)]. Under applied pressure, both scattering and absorption increase, which modulates the signal intensity detected by the PD.

Fig. 2(a) shows camera images of the contact region when a fingertip presses against a transparent glass plate. Comparison of cross-sectional intensity profiles between noncontact and contact states reveals an increase in RGB intensity during contact, which corresponds to a reduction in capillary blood volume [Fig. 2(b)]. The cross section along B–B′ confirms lateral expansion of the finger under applied load.

Several structural design considerations were implemented to enhance conformal skin contact. The skin-facing interface is primarily the FPC itself, minimizing the influence of the relatively rigid LED and PD packages on surface adhesion. The total stack thickness was maintained below 150 μm, allowing the device to conform to skin curvature and deformation even under relatively high loads. Because fingertips contain a high density of eccrine sweat glands, perspiration can lead to delamination and optical artifacts through additional scattering and absorption. To mitigate this, a small aperture was introduced between the emitter and the detector to promote sweat evaporation.
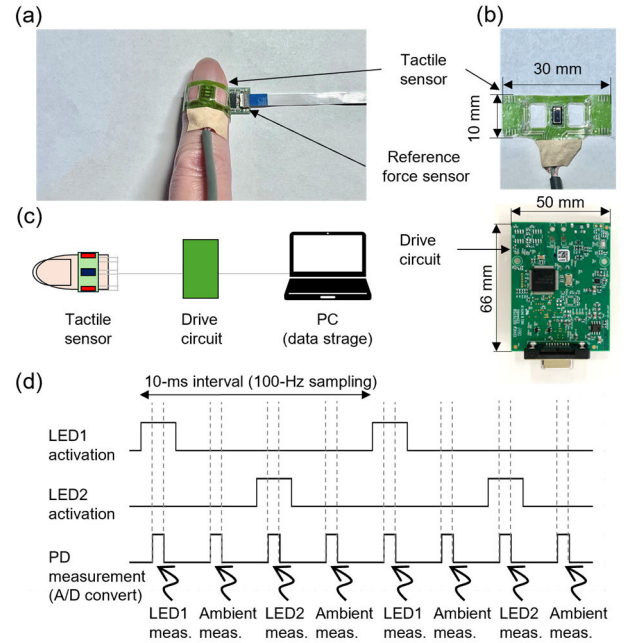

Fig. 3. Experimental setup for pressure measurement. (a) Sensor mounted on the finger together with a reference force sensor for ground-truth acquisition. (b) Structural components of the proposed sensor. (c) Measurement system consisting of the drive circuit, data acquisition unit, and personal computer. (d) Timing diagram of the LED and PD operation for synchronized optical signal acquisition.

Rather than directly using the raw sensor output, the device was designed with the assumption that multichannel optical signals would be processed by a downstream CNN. This approach compensates for variability arising from skin properties and attachment conditions while maintaining high pressure-estimation accuracy. In this sense, the device functions not only as an optical tactile sensor but also as an integrated tactile sensing system with a built-in calibration capability.

B. Experimental Setup

To evaluate the performance of the proposed optical tactile device with integrated calibration, we mounted the sensor on the dorsal side of the finger and constructed an experimental setup to apply known loads [Fig. 3(a) and (b)]. The prototype device was connected to a measurement board (AFE4403EVM, Texas Instruments) and interfaced with a Windows PC for data acquisition [Fig. 3(c)]. Parameter control and data logging were performed using a dedicated software tool (SLAC672, Texas Instruments). Signals under LED-on and LED-off conditions were sampled at 100 Hz for each channel [Fig. 3(d)].

As a reference, a high-precision six-axis force sensor (6DoF-P18, Touchence) was attached to the palmar side of the finger and measured concurrently with the optical signals. The contact area between the finger and the force sensor was kept constant throughout the measurements. The sensor was attached around the distal dorsal region of the finger, and repeated measurements were conducted under multiple loading conditions.

Loading was applied along the surface normal over a range of 0–100 kPa (0–4 N). Because the maximum tolerable load depends on the measurement site, the upper limit was adjusted based on local comfort and safety. Pressure was increased stepwise, and each step was held for 30 s to ensure steady-state acquisition. During measurements, the three-axis force components (Fx, Fy, Fz) from the reference sensor were synchronized with the optical channels (LED1 and LED2) to enable correspondence analysis.

All experiments were conducted under quasistatic conditions, with participants seated to minimize motion artifacts. Before attachment, the skin surface was cleaned, and the device was applied with visually aligned placement to emulate practical usage. To evaluate robustness, small positional offsets were intentionally introduced between repeated sessions. This study was approved by the Ethics Committee of Kobe University and conducted in accordance with the Declaration of Helsinki and institutional ethical guidelines.

C. Relationship Between Contact Force and Blood Flow

As shown in Fig. 2, increasing contact force deforms cutaneous tissue and simultaneously alters capillary blood volume, both of which directly influence the optical signals acquired by the sensor. The pressure-dependent dc component of the optical signal increases with load and saturates beyond a certain threshold [Fig. 4(a)]. This phenomenon has also been observed in previous studies. Sakuma et al. [34] demonstrated, using 3-D DIC measurements, that during pressing, the distal phalanx pulls the central region of the nail downward, while the subcutaneous tissue is displaced laterally and pushes up the nail edge from below, thereby elucidating the mechanism of fingertip tissue deformation under loading. Park et al. [35] used a sensor that measures pressure based on the lateral deformation of the finger pad and observed that the increase in sensor output gradually decreases as the applied force increases, quantitatively showing the saturation of fingertip tissue deformation by performing calibration with an exponential model. Shimawaki and Sakai [36] reported, through finite-element analysis based on CT images that the contact area rapidly increases in the low-load region and becomes nearly constant in the high-load region, demonstrating that the deformation of the skin and subcutaneous tissue saturates. These findings indicate that a similar phenomenon is likely occurring in this study. In contrast, the pulsatile ac component initially grows in amplitude and then diminishes at higher pressures as local perfusion decreases. Notably, the pulse rate remains nearly constant across loading conditions, indicating stable detection of pulsatile waves even under elevated pressure. This confirms that the sensor can capture physiological information concurrently with force evaluation.

External pressure affects not only amplitude but also the morphology of the pulse waveform [Fig. 4(b)]. The left panel shows that ac amplitude increases under light loads and decreases at high pressures, while the right panel displays normalized waveforms, revealing systematic variations in post-peak decay characteristics as force increases. These trends reflect the combined effects of tissue compression and altered microvascular hemodynamics. Taken together, the proposed
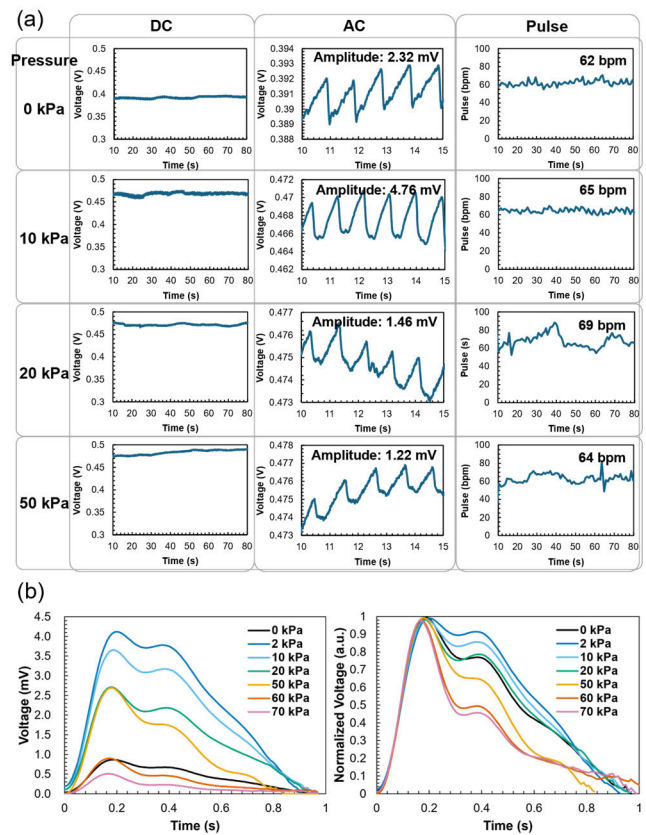

Fig. 4. Pressure-dependent optical response. (a) Variation of optical signal components with applied pressure: the dc level increases and gradually saturates, the ac amplitude initially rises and then decreases, while the pulse rate remains nearly constant. (b) Relationship between ac amplitude and pressure (left). Normalized pulse waveforms showing characteristic changes in amplitude and morphology with increasing pressure (right).

sensor captures both mechanical deformation and blood-flow dynamics through its dual optical channels.

Accordingly, this demonstrates that local blood flow changes induced by external forces can be detected noninvasively, suggesting the potential for applications in medical devices such as continuous blood pressure monitors and pulse oximeters, including vascular compliance assessment and compression-induced ischemia monitoring.

D. Data Acquisition and Preprocessing

This sensor exhibits structural characteristics in which its output varies substantially due to individual differences such as skin stiffness, geometry, vascular structure, and pulse–wave morphology, as well as slight positional shifts that alter the optical propagation path. Therefore, rather than constructing a fully generalized model, it is reasonable to ensure stable estimation accuracy by performing calibration and retraining at each attachment. The use case assumed in this study consists of the procedure from sensor attachment to the start of estimation as step 1 through step 4, with removal of the sensor included as step 5 in the overall sequence. An overview of these steps is shown in Fig. 5(a). Step 1: The user attaches the sensor to the measurement site using double-sided adhesive tape. Step 2: Calibration data are collected for several minutes
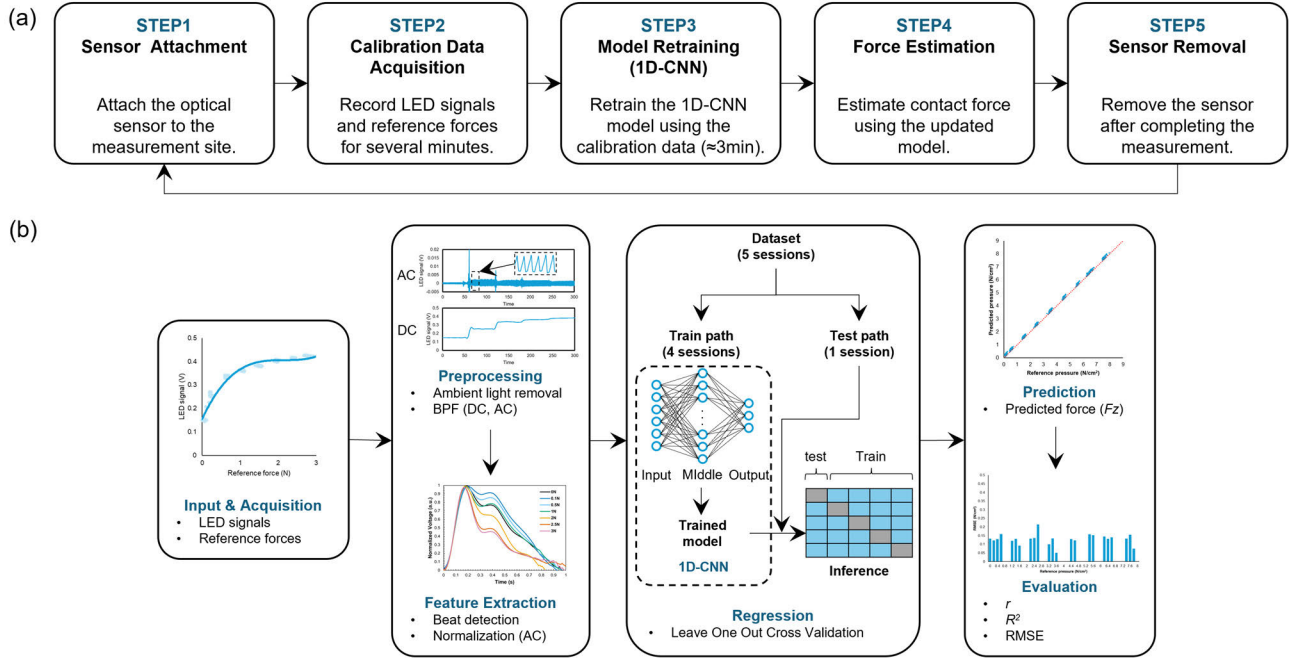
Fig. 5. Calibration and estimation workflow. (a) Operational workflow. Flow of sensor attachment, calibration-data acquisition, 1D-CNN retraining, force estimation, and sensor removal. (b) Analysis pipeline for CNN-based calibration. Flow of data acquisition, preprocessing, feature extraction, model training, and evaluation for pressure estimation.

using a reference sensor. Step 3: The collected calibration data are used to retrain the 1-D CNN (1D-CNN) model. The retraining time, including data transfer, is assumed to be within approximately 3 min. Step 4: The retrained 1D-CNN weights are applied to the sensor and estimation begins. Step 5: After the desired measurement duration, the sensor is removed, and the measurement is terminated.

To estimate contact force from the optical signals, we employed a CNN model [Fig. 5(b)]. The LED signals were preprocessed to extract dc and ac components. For each LED, signals recorded during illumination were sampled at 100 Hz, and ambient-light interference was removed by subtracting those obtained during LED-off periods. This yielded signal components attributable to tissue deformation and blood-flow variation. Even in the absence of external pressure, the signals exhibited pulsatile fluctuations corresponding to the cardiac cycle.

The differenced data were processed in Python. A fourth-order zero-phase Butterworth bandpass filter (0.05–30 Hz) was applied to suppress low-frequency motion artifacts and high-frequency noise. After windowing with a Hamming function, a fast Fourier transform (FFT) was performed to analyze spectral content, focusing on peaks within 0.5–1.5 Hz, corresponding to heart-rate-related pulsations. The dc component was obtained using a fourth-order low-pass filter with a 0.1 Hz cutoff, while the ac component was extracted using a fourth-order bandpass filter (0.5–5 Hz). The ac primarily reflected pulsatile information (PPG-like), whereas the dc captured baseline shifts associated with tissue deformation. These were analyzed alongside the reference forces (Fx, Fy, Fz).

Beat peaks in the ac component were detected using a Hilbert-transform-based squared envelope, smoothed with a 0.05-s window, and identified through a dynamic threshold

computed over a 0.8-s sliding window. To remove artifacts, intervals within ± 3 s of points where the derivative of Fz exceeded the 99th percentile were excluded as noise. Subsequent analyses were confined to valid beats outside these exclusion windows.

Each beat was normalized between 0 and 1 and resampled to a uniform grid to enable shape comparison. Beat-averaged Fz values were used to define 0.2-N bins, and within each bin, normalized waveforms were averaged to assess force-dependent morphology. From two LED channels, six inputs were prepared in total: dc, raw ac, and normalized ac signals for each LED.

A 1D-CNN regression model was constructed and trained on a per-recording basis.

E. Proposed CNN-Based Calibration Framework

The integrated calibration function processes six channels (dc, ac, and normalized ac from LED1 and LED2) to stabilize pressure estimation. A CNN was used to compensate for nonlinear variability caused by differences in finger size, vascular conditions, and attachment position. The CNN was trained as a regression model to estimate Fx, Fy, and Fz from the six input channels, using beat-wise averages of the reference force sensor as labels. The 1D-CNN consisted of two convolution-pooling blocks followed by fully connected layers that output three force components (Table I). Because real-time capability is required for pressure estimation, we adopted this configuration based on its low computational cost and fast inference performance. The 1D-CNN has a structure that can efficiently extract local features of time-series data through convolution operations and possesses the ability to flexibly accommodate changes in the shape and amplitude of the input waveforms. For this reason, even when the sensor output varies due to attachment position

TABLE I
ARCHITECTURE OF THE 1D-CNN MODEL USED FOR PRESSURE

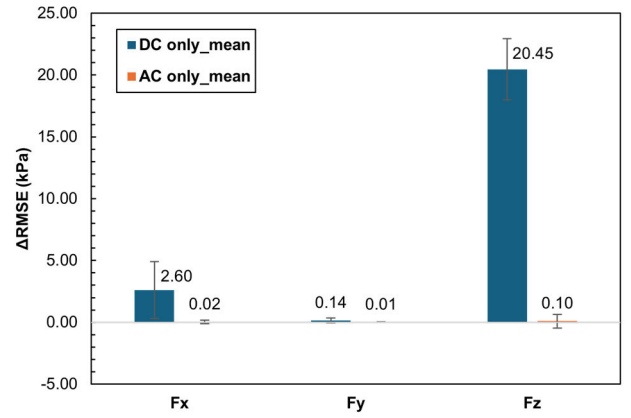| Layer	Parameters	Output shape
Input layer	6 units	[6] LED1(Fx, Fy, Fz), LED2(Fx, Fy, Fz)
Conv1 + ReLU	1D Conv, 32 filters, kernel=7	[32, T/2]
MaxPool1	Pool size=2	[32, T/2]
Conv2 + ReLU	1D Conv, 64 filters, kernel=7	[64, T/4]
MaxPool2	Pool size=2	[64, T/4]
Flatten	–	[64*(T/4)]
Dense + ReLU	128 units + Dropout(0.1)	[128]
Output layer	3 units	[3] Fx,Fy,Fz

Fig. 6. Ablation study of dc and ac components in the CNN model. ΔRMSE values obtained when estimating Fz using only the dc or only the ac component, computed as the RMSE difference relative to the condition using all components (dc + ac).

TABLE II
ESTIMATION ACCURACY ACROSS ALL FINGERS FROM
THUMB TO LITTLE FINGER

Fingertip		Thumb	Index	Middle	Ring	Little
Width	[mm]	2.1	1.5	1.6	1.4	1.2
Thickness	[mm]	1.6	1.2	1.3	1.2	1.1
Circumference	[mm]	6.3	4.9	5.2	4.8	4.1

or individual differences, we considered that stable pressure estimation could be achieved by enabling the model to capture diverse waveform patterns through learning.

Training was conducted with a batch size of 32, 32 epochs, and a learning rate of 0.001. Mean squared error (mse) served as the loss function, and optimization was performed using Adam. The dataset was divided 80/20 into training and validation sets, and the model with the lowest validation loss was used for evaluation.

The computational cost of the model was evaluated, and it was confirmed that approximately 1.06×10^6 MACs (about 2.1×10^6 FLOPs, assuming 1 MAC = 2 FLOPs) are required for a single inference. Based on this computational load, the inference time on typical mobile CPUs or embedded processors is estimated to be on the order of a few milliseconds, enabling real-time processing at a sampling rate of 100 Hz (10 ms period). Therefore, the 1D-CNN model used in this study has a lightweight structure that allows real-time estimation even under resource-constrained environments such as wearable devices, indicating its high practical potential from the perspective of computational cost.

F. Evaluation of Calibration Performance

To evaluate the effectiveness of the calibration function, we conducted five independent measurement sessions after attaching the sensor, alternating between training and inference phases using a leave-one-out (LOO) cross-validation framework. Each session served once as the evaluation fold, while the remaining sessions were used for training. This approach allowed assessment of generalization to variations in contact location and the relative composition of Fx, Fy, and Fz.

Although signal saturation was observed above approximately 40 kPa, which might affect training, we retained the entire range of 0–100 kPa (0–4 N) to evaluate model robustness even in the high-pressure region. Performance was assessed using the Pearson's correlation coefficient (r), the coefficient of determination (R^2), and the root-mean-square error (RMSE). RMSE was computed from the number of samples N, measured forces F_i, and estimated forces $\hat{F}_i$ as defined by the following equation:

$$\text{RMSE} = \sqrt{\frac{1}{N} \sum_{i=0}^{N-1} \left(F_i - \hat{F}_i \right)^2}. \qquad (1)$$

Because the contact area was constant, RMSE values in newtons were converted to pressure (kPa) for reporting. Additionally, the applied force was discretized into 0.1-N bins, and RMSE was calculated for each bin to quantify accuracy across the full pressure spectrum.

In addition, an ablation study was conducted as a preliminary examination to evaluate the contribution of the dc and ac components included in the input layer of the CNN model. In this analysis, estimation in the Fz direction was performed while disabling one of the components (ac or dc), and the difference in RMSE (ΔRMSE) from the case in which all inputs (dc+ac) were used was employed as an indicator of contribution. A load was applied in the Fz direction to the fingertip of the index finger, and five trials were conducted with the sensor attached; the mean and standard deviation of Fz were then calculated. As a result, the ΔRMSE was 20.45 ± 2.47 kPa when estimation was performed using only the dc component, and 0.10 ± 0.55 kPa when using only the ac component, indicating that the CNN model primarily utilizes the ac component for pressure estimation, with the dc component contributing in a supplementary manner (Fig. 6).

III. RESULTS

A. Pressure Estimation Performance Across Fingers

The sensor was mounted on all five digits (thumb, index, middle, ring, and little fingers) to evaluate how fingertip geometry affects estimation accuracy (Table II). For each attachment condition, five measurement sessions
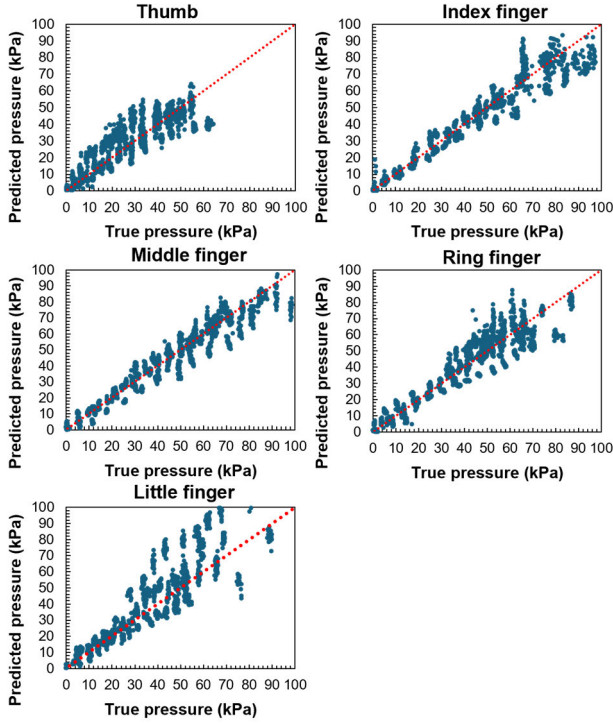
Fig. 7. Estimated versus reference forces for each finger. Scatter plots showing the relationship between estimated and measured forces for the thumb, index, middle, ring, and little fingers obtained from LOO cross-validation.

TABLE III
AGGREGATED ESTIMATION PERFORMANCE ACROSS ALL
FINGERS FROM THUMB TO LITTLE FINGER

Fingertip		Thumb	Index	Middle	Ring	Little
r	[-]	0.88	0.97	0.97	0.94	0.92
R^2	[-]	0.77	0.94	0.94	0.89	0.72
RMSE	[kPa] (N)	8.19 (0.35)	6.58 (0.28)	6.36 (0.27)	7.32 (0.31)	11.39 (0.49)

were conducted, and LOO cross-validation was employed to alternate between training and inference. Scatter plots of the estimated versus reference forces for each finger show that the predictions closely align with the line of identity, indicating strong agreement (Fig. 7). Statistical testing of the Pearson's correlation coefficient (r) yielded $p < 0.001$ for all five fingers. Because each evaluation fold contained more than 1000 samples, the correlations were statistically significant and reliable.

When aggregated across all five fingers, the coefficient of determination (R^2) ranged from 0.72 to 0.94, and the RMSE ranged from 6.36 to 11.39 kPa (0.27–0.49 N) (Table III). For context, these results were compared with previous studies that estimated pressure or force using sensors designed to avoid interference with natural tactile sensation (Table IV). Under this noninvasive condition, the proposed sensor achieved comparable or superior RMSEs, maintaining consistently high accuracy across all digits [6], [13], [35], [37], [38]. Although minor interfinger differences were observed, the overall

performance remained stable and did not depend on a specific finger. In a few cases, such as the thumb or little finger, accuracy slightly decreased and R^2 fell below 0.8; nevertheless, in 21 of 25 trials (84%), $R^2 \geq 0.8$, demonstrating robust estimation performance in the majority of measurements.

In addition, the sensor developed in this study applies minimal mechanical pressure to the skin, allowing it to be worn while maintaining natural tactile sensation, and it possesses multimodal sensing capability that enables simultaneous acquisition of physiological information through optical signals reflecting blood flow changes. These characteristics provide advantages over devices reported in previous studies in terms of both wearability and multifunctionality.

B. Pressure-Dependent Estimation Accuracy

To further evaluate performance across different force ranges, the contact force (Fz) for each finger was divided into 0.1-N bins (± 0.05 N), and RMSE was computed for each bin after converting force to pressure. Bins without samples were excluded from averaging because they do not represent valid error values.

Signal amplitude increased proportionally with applied pressure up to approximately 40 kPa, beyond which the response gradually saturated [Fig. 8(a)]. Although the onset of saturation varied slightly among fingers, three pressure regions could be identified: a linear region below 40 kPa, a transitional region between 40 and 60 kPa, and a fully saturated region above 60 kPa. The mean estimation error in each region is summarized in Fig. 8(b) and Table V.

Within the linear region, the sensor exhibited stable and accurate performance, with low-RMSE values typically within a few kilopascals. In the transitional region, partial saturation appeared in some fingers, leading to moderate increases in error. At higher pressures above 60 kPa, full saturation occurred in all fingers, and estimation accuracy gradually decreased; however, the RMSE remained within a practically acceptable range, on the order of 10–15 kPa (approximately 0.4–0.6 N).

C. Effect of Sensor Positional Shift

To assess robustness against reattachment, the sensor was deliberately shifted laterally when mounted on the finger. The nominal position aligned the center of the PD with the longitudinal axis of the finger. Three conditions were compared: nominal position and ± 2 mm lateral offsets relative to nominal [Fig. 9(a) and (b)]. The sensor position affected the relative intensities of LED1 and LED2. At the center position, their outputs were nearly equal; when shifted 2 mm to the left, LED2 intensity exceeded LED1, whereas a 2-mm right shift resulted in the opposite trend [Fig. 9(c)].

Although reattachment introduced small variations in signal amplitude and baseline, both the Pearson's correlation coefficient (r) and the coefficient of determination (R^2) remained high under all conditions [Fig. 9(d)]. Statistical testing yielded $p < 0.001$ for all three mounting conditions, confirming the reliability of the correlations, as each evaluation contained more than 1000 samples. Furthermore, RMSE was less than

TABLE IV
COMPARISON WITH PREVIOUS STUDIES

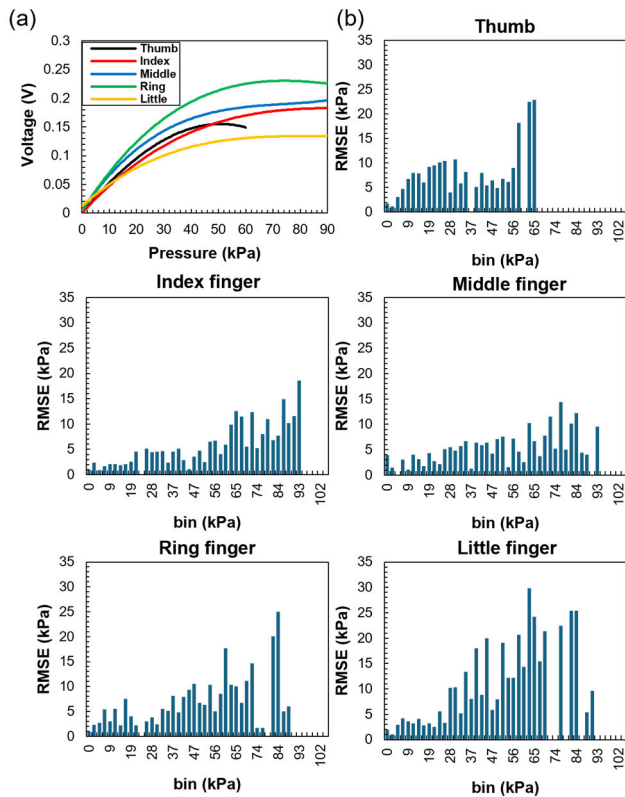| [Ref.]	[Sensor]	[Maxima force range, in N] Normal force : Fz	[RMSE, in N]	[Sensor adaptability] Low Skin Pressure during Attachment	[Sensor adaptability] multimodal capability: physiological data
–	**LEDs and photodiode**	**4**	**Thumb:0.35, Index:0.28, Middle:0.27, Ring:0.31, Little:0.49**	**Yes**	**Yes**
[6]	Camera	8	0.55	Yes	No
[13]	LEDs and photodiodes	10	1.179	Yes	No
[35]	Capacitive force sensors	5	Thumb: 0.796, Index: 0.843, Middle: 0.261	No	No
[37]	Optical sensors and IMU	10-15 (over 90% below 6 N)	Thumb:1.70, Index:1.95, Middle:1.34, Ring:1.28, Little:1.56	No	No
[38]	Piezoresistive bend sensor	5	0.53	No	No

Fig. 8. Pressure-dependent response and estimation error. (a) Signal amplitude as a function of applied pressure for each finger. (b) Distribution of RMSE across pressure bins for all fingers.

TABLE V
MEAN RMSE VALUES FOR EACH PRESSURE
RANGE ACROSS FINGERS

Force range		Thumb	Index	Middle	Ring	Little
0-40 kPa (0-1.7 N)	[kPa] (N)	6.63 (0.29)	3.06 (0.13)	3.72 (0.16)	4.03 (0.17)	5.74 (0.25)
40-60 kPa (1.7-2.6 N)	[kPa] (N)	8.12 (0.35)	4.01 (0.17)	5.58 (0.24)	8.08 (0.35)	13.35 (0.57)
≧ 60 kPa (≧ 2.6 N)	[kPa] (N)	22.64 (0.97)	10.1 (0.43)	7.68 (0.33)	10.84 (0.47)	19.31 (0.83)

Fig. 9. Effect of sensor positional shift. (a) Sensor locations at −2, 0, and +2 mm relative to the finger center. (b) Cross-sectional views corresponding to the positions shown in (a). (c) LED output intensities at each position. (d) Scatter plots of estimated versus reference pressures.

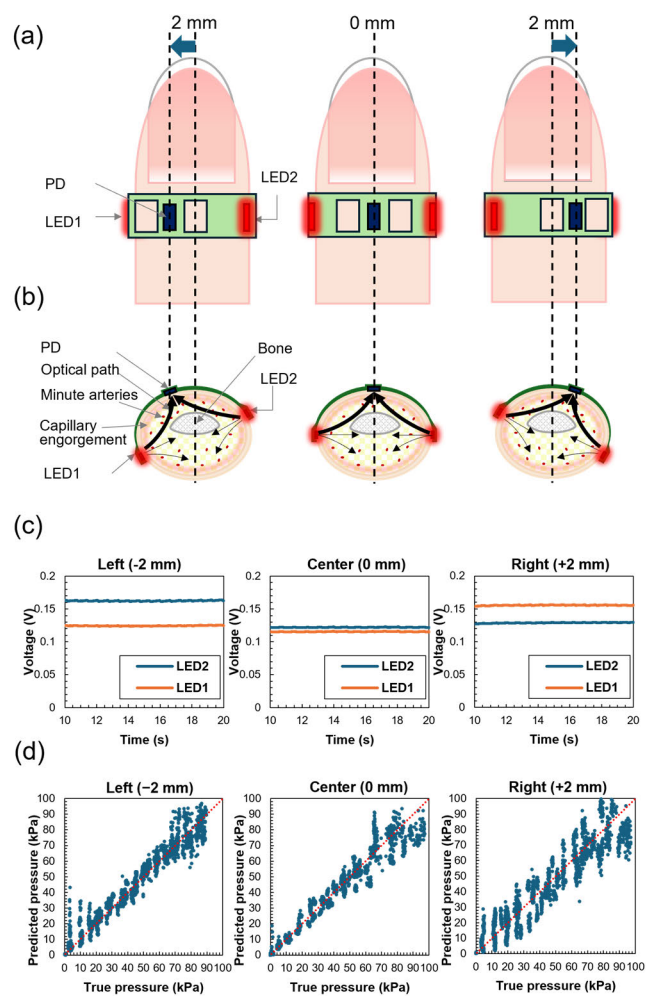10 kPa in every condition, and no significant increase in error was observed after reattachment (Table VI). These results demonstrate that the proposed calibration function effectively compensates for local positional misalignment, ensuring stable estimation performance under realistic re-donning conditions.

TABLE VI
ESTIMATION ACCURACY UNDER DIFFERENT ATTACHMENT POSITIONS

Fingertip (Index finger)		Left (= -2 mm)	Center (= 0 mm)	Right (= +2 mm)
r	[-]	0.98	0.97	0.94
R^2	[-]	0.96	0.94	0.89
RMSE	[kPa] (N)	5.67 (0.24)	6.58 (0.28)	9.70 (0.42)

TABLE VII
ESTIMATION ACCURACY ACROSS SUBJECTS

Fingertip (Index finger)		Subject 1	Subject 2	Subject 3
r	[-]	0.97	0.86	0.89
R^2	[-]	0.94	0.73	0.71
RMSE	[kPa] (N)	6.58 (0.28)	12.16 (0.52)	11.33 (0.49)

D. Reproducibility and Intersubject Variability

Reproducibility within subjects and variability across subjects were assessed using three participants (two male and one female, ages in their 20–30 s). Each participant wore the sensor on the index finger and completed five independent measurement sessions under identical conditions without re-donning. LOO cross-validation was applied, using each session once as the validation fold.

For each participant, the Pearson's correlation coefficient (r), the coefficient of determination (R^2), and the RMSE were computed for pressure estimation (Table VII). Statistical testing of r yielded $p < 0.001$ for all participants, confirming statistical significance. Although R^2 and RMSE varied slightly among individuals, all participants exhibited consistent estimation behavior. Subject 1 achieved the highest accuracy, while the remaining subjects maintained $R^2 \geq 0.7$, indicating stable generalization across different individuals. RMSE values ranged from 6.58 to 12.16 kPa (0.28–0.52 N), which is comparable to or better than those reported in previous studies (Table V). Collectively, these results demonstrate that the CNN-based calibration framework achieves reliable, subject-independent performance and maintains generalization across users with different finger geometries and physiological characteristics.

IV. DISCUSSION

Building upon a flexible optical tactile sensor that estimates pressure from skin deformation and blood flow changes, we developed a CNN-based calibration framework that enables stable force estimation insensitive to placement variability and intersubject differences. By limiting the sensor thickness to less than 150 μm and incorporating an aperture structure, the design suppresses sweat-induced delamination while maintaining comfort and stable skin contact during prolonged wear. These features allow the sensor to acquire force information

without interfering with natural tactile sensation, making it highly suitable for wearable applications.

In experimental evaluations, the proposed model consistently achieved high accuracy across all fingers, with R^2 values typically between 0.7 and 0.9 and RMSE values below approximately 12 kPa (0.5 N) throughout the 0–100 kPa (0–4 N) range. Even when the sensor was intentionally shifted from its nominal position, estimation accuracy remained stable, confirming robustness against positional variation. Comparable performance was also observed across different subjects, indicating that the CNN-based calibration effectively compensates for differences in skin properties, vascular conditions, and attachment configuration.

In the high-pressure region (above approximately 40 kPa), signal saturation was observed along with an increase in RMSE. This phenomenon likely occurs because tissue compression and reduced blood volume alter the optical scattering and absorption properties, leading to nonlinear signal behavior. Nevertheless, characteristic changes in the amplitude and morphology of the pulsatile waveform appeared at higher loads, indicating that the sensor concurrently captures hemodynamic variations with mechanical deformation. Therefore, unlike conventional devices that measure only pressure magnitude, the proposed sensor can simultaneously acquire biomechanical (skin deformation) and physiological (blood flow dynamics) information, providing an integrated platform for multimodal sensing.

In addition, because actual grasping tasks involve oblique loading and shear forces acting simultaneously, a preliminary evaluation was conducted to examine the estimation accuracy for components other than the axial direction. Under conditions in which shear force (Fx) was applied up to a maximum of 1 N, five evaluations using LOO were performed, resulting in an R^2 of 0.75 and RMSE of 2.96 kPa (0.127 N). In contrast, when axial force (Fz) was applied up to 1 N under the same conditions, the results were R^2 of 0.92 and RMSE of 1.9 kPa (0.08 N). These findings indicate that the estimation accuracy for shear components is lower than that for the axial direction. Future work will focus on improving robustness in multiaxial force estimation by enhancing accuracy with respect to loading direction, for example, through structural modifications such as multipoint arrangements of the emitters or the detectors.

Across participants, the correlations between estimated and reference pressures remained consistently high, typically yielding R^2 values around 0.8. Although perfect agreement was not achieved, this deviation can be attributed to interindividual differences in skin stiffness, optical scattering, and vascular distribution, as well as minor variations in sensor placement and orientation relative to the skin, which influence photon propagation and reflected intensity.

Future improvements can be achieved in several directions. First, optimizing the layout of the optical elements to homogenize the sensitivity field could reduce position-dependent variations. Second, adopting multiwavelength and multisite illumination/detection may enable simultaneous probing of superficial and deep tissue layers, enhancing both force estimation and blood-flow analysis. Third, model generalization could be further improved by introducing subject-adaptive

learning or transfer-learning approaches. Finally, implementing wireless communication (e.g., Bluetooth low energy) would enhance mobility and comfort, facilitating continuous and practical use in wearable scenarios.

Quantitative assessment of tactile information is valuable not only in robotics and human–machine interfaces but also in biomechanics, rehabilitation, and consumer product evaluation. The calibration approach proposed in this study improves reproducibility and quantitative reliability by compensating for interindividual and attachment-related variability. Consequently, it supports applications such as safe and precise grasp control in collaborative robots and quantitative skill assessment in sports and cosmetic manipulation. More broadly, the proposed system represents a general-purpose platform that enables quantitative analysis of both mechanical and physiological information through tactile sensing.

V. Conclusion

This study presented a flexible optical tactile sensor equipped with a CNN-based calibration framework capable of estimating pressure from optical signals associated with skin deformation and blood flow dynamics. The proposed approach achieved stable and high-accuracy estimation across different fingers, attachment conditions, and individuals. In all experiments, the coefficient of determination generally ranged around 0.8, and the RMSE remained within approximately 10 kPa (0.4 N), demonstrating robustness and reliable generalization.

By combining mechanical and physiological sensing within a thin, lightweight, and skin-conformal structure, the sensor provides pressure estimation without obstructing natural tactile sensation. The integrated calibration effectively compensates for positional and subject-dependent variability, enabling reproducible and quantitative tactile measurement.

The versatility of the proposed system suggests broad potential applications. In robotics, it can enhance safe and adaptive force control for collaborative robots. In biomedical and wearable contexts, it enables continuous monitoring of contact pressure and hemodynamic responses during rehabilitation or daily activities. Furthermore, the ability to simultaneously capture mechanical and physiological information opens new opportunities for multimodal human sensing and tactile analytics.

Future work will focus on extending the sensing range, improving model generalization through adaptive learning and integrating wireless communication for real-time monitoring. Collectively, these developments aim to establish a practical and scalable tactile-sensing platform that bridges human and robotic touch perception.

References

[1] Y. Luo et al., "Adaptive tactile interaction transfer via digitally embroidered smart gloves," *Nature Commun.*, vol. 15, no. 1, p. 868, Jan. 2024.

[2] K. Kim, H. Yang, J. Lee, and W. G. Lee, "Metaverse wearables for immersive digital healthcare: A review," *Adv. Sci.*, vol. 10, no. 31, Nov. 2023, Art. no. 2303234.

[3] P. Sathe, A. Schmitz, T. P. Tomo, S. Somlor, S. Funabashi, and S. Shigeki, "FingerTac—An interchangeable and wearable tactile sensor for the fingertips of human and robot hands," in *Proc. IEEE/RSJ Int. Conf. Intell. Robots Syst. (IROS)*, Detroit, MI, USA, Oct. 2023, pp. 10813–10820.

[4] R. Cobo, J. García-Piqueras, J. Cobo, and J. A. Vega, "The human cutaneous sensory corpuscles: An update," *J. Clin. Med.*, vol. 10, no. 2, p. 227, Jan. 2021.

[5] A. Zimmerman, L. Bai, and D. D. Ginty, "The gentle touch receptors of mammalian skin," *Science*, vol. 346, no. 6212, pp. 950–954, Nov. 2014.

[6] R. Ono, S. Yoshimoto, and K. Sato, "Visual force sensing for deviceless interface with finger pushing onto palm," *J. Inst. Image Inf. Telev. Engineers*, vol. 68, no. 7, pp. J285–J291, 2014.

[7] M. Nakatani and T. Kawasoe, "Haptic skill logger (HapLog): The wearable sensor for evaluating haptic behaviors," *J. Robot. Soc. Jpn.*, vol. 30, no. 5, pp. 499–501, 2012.

[8] S. A. Mascaro and H. H. Asada, "Understanding of fingernail-bone interaction and fingertip hemodynamics for fingernail sensor design," in *Proc. 10th Symp. Haptic Interface Virtual Environ. Teleoperator Syst. HAPTICS*, Mar., pp. 106–113.

[9] J. Chen et al., "Three-dimensional arterial pulse signal acquisition in time domain using flexible pressure-sensor dense arrays," *Micromachines*, vol. 12, no. 5, p. 569, May 2021.

[10] M. S. Sarwar et al., "Touch, press and stroke: A soft capacitive sensor skin," *Sci. Rep.*, vol. 13, no. 1, p. 17390, Oct. 2023.

[11] G. Vega et al., "VARitouch: Back of the finger device for adding variable compliance to rigid objects," in *Proc. CHI Conf. Human Factors Comput. Syst.*, New York, NY, USA, May 2024, pp. 1–20.

[12] H. Mameno, M. Imura, Y. Uranishi, S. Yoshimoto, and O. Oshiro, "Estimation of fingertip contact force direction based on change in nail color distribution," *Jpn. J. Med. Eng.*, vol. 52, pp. O-155–O-156, Jan. 2014.

[13] A. Saito, W. Kuno, W. Kawai, N. Miyata, and Y. Sugiura, "Estimation of fingertip contact force by measuring skin deformation and posture with photo-reflective sensors," in *Proc. 10th Augmented Hum. Int. Conf.*, New York, NY, USA, Mar. 2019, pp. 1–6.

[14] E. Andreozzi et al., "Multimodal finger pulse wave sensing: Comparison of forcecardiography and photoplethysmography sensors," *Sensors*, vol. 22, no. 19, p. 7566, Oct. 2022.

[15] T. W. Kang et al., "Soft nanomembrane sensor-enabled wearable multimodal sensing and feedback system for upper-limb sensory impairment assistance," *ACS Nano*, vol. 19, no. 5, pp. 5613–5628, Feb. 2025.

[16] K. Ando, M. Kushihashi, H. Kawaguchi, and S. Izumi, "Flexible optical tactile force sensor to conduct measurements from the back of the hand," *IEEE Sensors J.*, vol. 25, no. 8, pp. 12872–12880, Apr. 2025.

[17] A. B. Hertzman, "The blood supply of various skin areas as estimated by the photoelectric plethysmograph," *Amer. J. Physiol.-Legacy Content*, vol. 124, no. 2, pp. 328–340, Oct. 1938.

[18] H. Jinno et al., "Self-powered ultraflexible photonic skin for continuous bio-signal detection via air-operation-stable polymer light-emitting diodes," *Nature Commun.*, vol. 12, no. 1, p. 2234, Apr. 2021.

[19] S. Park et al., "Ultraflexible near-infrared organic photodetectors for conformal photoplethysmogram sensors," *Adv. Mater.*, vol. 30, no. 34, Aug. 2018, Art. no. e1802359.

[20] G. Simone et al., "High-accuracy photoplethysmography array using near-infrared organic photodiodes with ultralow dark current," *Adv. Opt. Mater.*, vol. 8, no. 10, May 2020, Art. no. 1901989.

[21] H. Lee et al., "Toward all-day wearable health monitoring: An ultralow-power, reflective organic pulse oximetry sensing patch," *Sci. Adv.*, vol. 4, no. 11, p. 9530, Nov. 2018.

[22] J. L. Bowden and P. A. McNulty, "Age-related changes in cutaneous sensation in the healthy human hand," *AGE*, vol. 35, no. 4, pp. 1077–1089, Aug. 2013.

[23] B. Li and G. J. Gerling, "An individual's skin stiffness predicts their tactile discrimination of compliance," *J. Physiol.*, vol. 601, no. 24, pp. 5777–5794, Dec. 2023.

[24] J. Allen, "Photoplethysmography and its application in clinical physiological measurement," *Physiolog. Meas.*, vol. 28, no. 3, pp. R1–R39, Feb. 2007.

[25] H. Shin, G. Noh, and B.-M. Choi, "Photoplethysmogram based vascular aging assessment using the deep convolutional neural network," *Sci. Rep.*, vol. 12, no. 1, p. 11377, Jul. 2022.

[26] P. W. Egger, G. L. Srinivas, and M. Brandstötter, "Real-time detection and localization of force on a capacitive elastomeric sensor array using image processing and machine learning," *Sensors*, vol. 25, no. 10, p. 3011, May 2025.

[27] X. Zhang, S. Li, J. Yang, Y. Wang, Z. Huang, and J. Zhang, "Tactile perception object recognition based on an improved support vector machine," *Micromachines*, vol. 13, no. 9, p. 1538, Sep. 2022.

[28] B. Shih et al., "Electronic skins and machine learning for intelligent soft robots," *Sci. Robot.*, vol. 5, no. 41, p. 9239, Apr. 2020.

[29] C. Jiang et al., "Capturing forceful interaction with deformable objects using a deep learning-powered stretchable tactile array," *Nature Commun.*, vol. 15, no. 1, p. 9513, Nov. 2024.

[30] A. M. M. Almassri, W. Z. W. Hasan, S. A. Ahmad, S. Shafie, C. Wada, and K. Horio, "Self-calibration algorithm for a pressure sensor with a real-time approach based on an artificial neural network," *Sensors*, vol. 18, no. 8, p. 2561, Aug. 2018.

[31] T. G. Thuruthel, B. Shih, C. Laschi, and M. T. Tolley, "Soft robot perception using embedded soft sensors and recurrent neural networks," *Sci. Robot.*, vol. 4, no. 26, p. 1488, Jan. 2019.

[32] D. Kim, J. Kwon, B. Jeon, and Y.-L. Park, "Adaptive calibration of soft sensors using optimal transportation transfer learning for mass production and long-term usage," *Adv. Intell. Syst.*, vol. 2, no. 6, Jun. 2020, Art. no. 1900178.

[33] E. Ayodele et al., "Grasp classification with weft knit data glove using a convolutional neural network," *IEEE Sensors J.*, vol. 21, no. 9, pp. 10824–10833, May 2021.

[34] K. Sakuma et al., "Wearable nail deformation sensing for behavioral and biomechanical monitoring and human-computer interaction," *Sci. Rep.*, vol. 8, no. 1, p. 18031, Dec. 2018.

[35] J. Park, P. Heo, J. Kim, and Y. Na, "A finger grip force sensor with an open-pad structure for glove-type assistive devices," *Sensors*, vol. 20, no. 1, p. 4, Dec. 2019.

[36] S. Shimawaki and N. Sakai, "Quasi-static deformation analysis of a human finger using a three-dimensional finite element model constructed from CT images," *J. Environ. Eng.*, vol. 2, no. 1, pp. 56–63, 2007.

[37] S. Miyake and T. Miyake, "Force estimation of five fingers using infrared optical sensors and an IMU and its application to analysis of sports motion," *IEEE Sensors J.*, vol. 25, no. 6, pp. 10122–10133, Mar. 2025.

[38] T. Ozaki, N. Ohta, and M. Fujiyoshi, "Highly sensitive and easy-to-attach wearable sensor for measuring finger force based on curvature changes in an ellipse-shaped finger ring," *Smart Mater. Struct.*, vol. 33, no. 7, Jul. 2024, Art. no. 077001.

Hiroshi Kawaguchi (Member, IEEE) received the B.Eng. and M.Eng. degrees in electronic engineering from Chiba University, Chiba, Japan, in 1991 and 1993, respectively, and the Ph.D. degree in electronics engineering from The University of Tokyo, Tokyo, Japan, in 2006.

In 1993, he joined the Konami Corporation, Kobe, Japan, where he developed arcade entertainment systems. In 1996, he joined the Institute of Industrial Science, The University of Tokyo, as a Technical Associate, and was appointed as a Research Associate, in 2003. In 2005, he joined the Graduate School of Engineering, Kobe University, Kobe, as a Research Associate. From 2015 to 2016, he was a Visiting Researcher with Politecnico di Milano, Milan, Italy. Since 2016, he has been a Full Professor at the Graduate School of Science, Technology and Innovation, Kobe University. He is also a Collaborative Researcher with the Institute of Industrial Science, The University of Tokyo. His current research interests include low-voltage operating circuits, soft error characterization and mitigation, ubiquitous sensor networks, organic semiconductor circuits, data converters, healthcare devices, and neurocomputer architecture.

Dr. Kawaguchi is a member of ACM and IEICE. He was a recipient of the IEEE ISSCC 2004 Takuo Sugano Outstanding Paper Award, the ACM/IEEE ASP-DAC 2013 University Design Contest Best Design Award, and the IEEE ICECS 2016 Best Paper Award. He has served as a Design and Implementation of Signal Processing Systems (DISPS) Technical Committee Member for IEEE Signal Processing Society; a Technical Program Committee Member for IEEE International Conference on Acoustics, Speech and Signal Processing (ICASSP), IEEE Global Conference on Signal and Information Processing (GlobalSIP), IEEE Workshop on Signal Processing Systems (SiPS), IEEE Custom Integrated Circuits Conference (CICC), and IEEE Symposium on Low-Power and High-Speed Chips (COOL Chips); and an Organizing Committee Member for IEEE Asian Solid-State Circuits Conference (A-SSCC) and ACM/IEEE Asia and South Pacific Design Automation Conference (ASP-DAC). He was an Associate Editor of the *Journal of Signal Processing Systems* (Springer), *IEICE Transactions on Fundamentals of Electronics, Communications and Computer Sciences*, *IEICE Transactions on Electronics*, and *IPSJ Transactions on System LSI Design Methodology* (TSLDM).

Shintaro Izumi (Member, IEEE) received the B.Eng. and M.Eng. degrees in computer science and systems engineering and the Ph.D. degree in engineering from Kobe University, Kobe, Hyogo, Japan, in 2007, 2008, and 2011, respectively.

From 2009 to 2011, he was a JSPS Research Fellow at Kobe University, an Assistant Professor with the Organization of Advanced Science and Technology, Kobe University, from 2011 to 2018, and an Associate Professor with the Institute of Scientific and Industrial Research, Osaka University, Suita, Japan, from 2018 to 2019. Since 2019, he has been an Associate Professor with the Graduate School of System Informatics, Kobe University. His current research interests include biomedical signal processing, communication protocols, low-power VLSI design, and sensor networks.

Dr. Izumi has served as a Technical Committee Member for IEEE Biomedical and Life Science Circuits and Systems, a Student Activity Committee Member for IEEE Kansai Section, and a Program Committee Member for IEEE Symposium on Low-Power and High-Speed Chips (COOL Chips). He was a recipient of the 2010 IEEE SSCS Japan Chapter Young Researchers Award. He was the Chair of the IEEE Kansai Section Young Professionals Affinity Group.

Kosuke Ando received the B.Eng. degree in energy science and engineering and the M.Eng. degree in applied quantum physics and nuclear engineering from Kyushu University, Fukuoka, Japan, in 2013 and 2015, respectively. He is currently pursuing the Ph.D. degree with the Graduate School of Science, Technology, and Innovation, Kobe University, Kobe, Japan.

In 2015, he joined KONICA MINOLTA, Inc., Tokyo, Japan, where he developed optical devices. His current research interests include biosensing technology.